Journal of
Materials Chemistry C

PAPER

View Article Online
View Journal | View Issue

Check for updates

Cite this: *J. Mater. Chem. C*, 2022, **10**, 1999

White-light defect emission and enhanced photoluminescence efficiency in a 0D indium-based metal halide†

Qidi Ran, Yan Zhang, Jun Yang, Rongxing He,* Lei Zhou* and Shanshan Hu*

Received 25th October 2021,
Accepted 12th January 2022

DOI: 10.1039/d1tc05140g

rsc.li/materials-c

Low-dimensional ns^2-metal halide compounds with confined structures and localized electronic states have received considerable attention due to their superior luminescence properties, while the intriguing photophysical dynamics of metal halides without ns^2 electrons is still elusive and has yet to be investigated. Herein, we have developed a novel In^{3+}-based $(C_6H_8N)_6InBr_9$ single crystal that exhibits intrinsic white-light emission at room temperature. Such white light stems from multiple defect states owing to the presence of Br vacancies, which however delivers a low photoluminescence quantum yield (PLQY) (2.72%) due to a severe thermal quenching effect. To improve the photoluminescence efficiency, the Sb^{3+} ion with a 5s^2 lone pair has been embedded into the lattice, which leads to broadband orange emission with a high PLQY of up to 71.84%. The enhanced PL efficiency results from efficient triplet self-trapped excitons (STEs) in the $(SbBr_6)^{3-}$ octahedron and the energy transfer from defect states to STE states. This work not only sheds light on the mechanism of defect-related white-light emission, but provides a successful strategy for designing novel materials with excellent PL properties for versatile optical applications.

Introduction

Lead halide perovskites have emerged as one of the most promising classes of light absorbers for low-cost, efficient solar cells.[1–3] Their exceptional electronic and optical properties also encourage researchers to explore potential applications beyond solar cells.[4–8] In particular, low-dimensional organic–inorganic metal halides have been considered as efficient emitters due to the merits of structural and compositional tunability, extraordinary optical properties and facile synthesis by wet and solid-state methods,[9–17] which are potentially used in display technologies, solid-state lighting, scintillators, remote thermography and anti-counterfeiting labeling.[18–25] Notwithstanding the rapid advance in materials' diversity and photoluminescence (PL) efficiency, their fundamental photophysical mechanisms are still elusive, which needs to be clarified not only from a basic science point of view, but for the purpose of designing novel materials with exceptional PL properties for practical applications.

The dimensions and optical properties of organic–inorganic hybrid metal halides can be tuned by selection of the metal, halogen, and organic components.[26–29] As the structural dimensionality or electronic structures decrease, excited state carriers are more easily localized within the anionic entities, thereby promoting the radiative recombination. In this regard, electronic localization culminates in zero-dimensional (0D) metal halides whose anionic entities are not connected (*i.e.*, completely isolated), which provides hints about some of the unique properties such as large (>150 meV) exciton binding energy, ultra-broadband emission (>60 nm), large Stokes shift (>100 nm) and remarkable PL quantum yields (PLQYs).[30–33] For the generation of broadband PL, the widely accepted mechanism is due to radiative recombination of self-trapped excitons (STEs) in ns^2-metals (Pb^{2+}, Sn^{2+}, Sb^{3+}, *etc.*), as a consequence of strong coupling between photogenerated excitons and "soft" lattices;[26] for instance, 0D material $(C_9NH_{20})_7(PbCl_4)$-$Pb_3Cl_{11}\cdot CH_3CN$ with a PLQY of 83% and a full width at half maximum (FWHM) of 84 nm,[34] Bmpip$_2$PbBr$_4$ with a PLQY of 75% and a FWHM over 300 nm,[21] and $(C_9NH_{20})_2SbCl_5$ with a near-unity PLQY and a FWHM of 119 nm.[35] Besides, broadband PL can also result from defect-assisted recombination due to the presence

---

Key Laboratory of Luminescence Analysis and Molecular Sensing (Southwest University), Ministry of Education, School of Chemistry and Chemical Engineering, Southwest University, Chongqing, 400715, P. R. China. E-mail: herx@swu.edu.cn, zhoulei25@swu.edu.cn, hushan3@swu.edu.cn

† Electronic supplementary information (ESI) available: Additional supplementary figures and tables showing single crystal X-ray diffraction measurements, PXRD measurements, ICP-OES measurements, PL measurements, PL lifetime measurements, thermogravimetric analysis, SEM-EDX, UV-vis absorption and PLQY measurements. CCDC 2119939. For ESI and crystallographic data in CIF or other electronic format see DOI: 10.1039/d1tc05140g

of lattice defects in the anionic entity. For the ionic-type bulk metal halides, halide/metal vacancies, interstitials, and antisites are common structural defects in the formation of bulk assemblies,[36] while surface defects are neglectable because of the high crystallinity of the materials. The formed shallow and deep defects in the band gap play different roles in determining the materials' photophysical processes, and it is known that the deep-level defects might be nonradiative recombination centers, shortening the carrier lifetimes and deteriorating the optical properties, while the shallow-level defects may be PL centers.[37–42] Nevertheless, reports on 0D metal halides with defect-assisted PL are rare,[43–45] and the understanding of the defect properties in this type of material is still in its infancy; thus, there remain many open questions to be solved.

Luminescent lead-free indium (In)-based materials have attracted growing interest recently due to their air and photostability and the excellent optoelectronic properties.[9,20,46–52] In contrast to ns^2-metals with an outer-shell lone pair, In^{3+} has a filled 4d^{10}5s^0 electron configuration, which makes its compound as an ideal prototype to unveil the intriguing photophysical mechanism. Thus, in this work, we concentrate on the broad emission from 0D In^{3+}-based halides. We report a novel In^{3+}-based $(C_6H_8N)_6InBr_9$ single crystal with a 0D structure, which exhibits intrinsic broadband white emission spanning from 400 to 725 nm. Experimental characterizations reveal that the white light originates from multiple defect states associated with the Br vacancies in the lattice. Interestingly, incorporating a trace amount of Sb^{3+} into the $(C_6H_8N)_6InBr_9$ lattice can induce intensive broadband emission ranging from the green to near infrared (NIR) regions, with a high PLQY of up to ~71.84%. Such efficient broadband PL is attributed to extrinsic STEs that arise from the triplet emission state of the $(SbBr_6)^{3-}$ octahedron and the strong exciton–phonon coupling. Moreover, the efficient energy transfer from defect levels to the triplet state of Sb^{3+} also contributes to the enhanced PL efficiency.

Results and discussion

Colorless needle-like $(C_6H_8N)_6InBr_9$ single crystals were prepared using C_6H_9NBr and $InBr_3$ in hydrobromic acid by a hydrothermal method (Fig. S1, ESI†). Single-crystal X-ray diffraction measurement manifests that $(C_6H_8N)_6InBr_9$ crystallizes in a periodic 0D structure at the molecular level, with monoclinic space group *I*2/*a* (cell parameters a = 9.97 Å, b = 21.47 Å, c = 23.09 Å, $\alpha = \gamma = 90°$, and β = 92.96°). (More details are presented in Table S1, ESI†.) In this structure, each In is coordinated with six Br to form an octahedron that is isolated by six $C_6H_9N^+$ and three uncoordinated Br$^-$, as demonstrated in Fig. 1a and b. Details of the structure in Fig. S2 (ESI†) reveal that the $(InBr_6)^{3-}$ octahedron exhibits a Jahn–Teller-like distortion with the equatorial bonds lengthened up to 0.93%, which probably has an impact on its photophysical processes. The distance between two adjacent In atoms is more than 9.97 Å, indicating no electronic interaction between two adjacent metal–halide octahedra (Fig. S3, ESI†). The powder X-ray diffraction (PXRD) pattern of the ball-milled powders of the single crystals matches well with the simulated PXRD pattern (Fig. 1c), verifying its high phase purity. The Fourier transform infrared spectrum of $(C_6H_8N)_6InBr_9$ contains the characteristic absorption peaks of the organic cation, confirming that the organic cations have been successfully embedded in the crystal structure (Fig. S4, ESI†). The morphology of $(C_6H_8N)_6InBr_9$ single crystals was characterized by scanning electron microscopy (SEM). As shown in Fig. S5 (ESI†), the crystals crystallize in needle-like shapes with homogeneous element distributions of In and Br. The corresponding energy dispersive X-ray spectroscopy (EDS) reveals that the ratio of Br/In is 8.5/1, suggesting that the crystals are slightly deficient in Br, which arises possibly due to the halogen release during the process of crystallization.

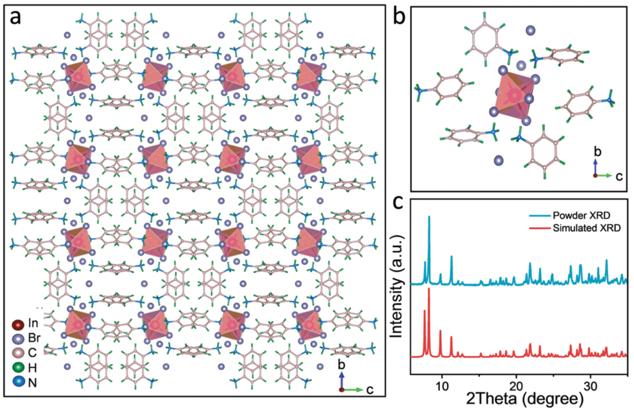

Fig. 1 (a) A 2 × 2 × 2 super cell crystal structure of the $(C_6H_8N)_6InBr_9$ along the *a* axis. (b) Detailed view of the crystal structure of $(C_6H_8N)_6InBr_9$. (c) PXRD pattern and the corresponding simulated data of $(C_6H_8N)_6InBr_9$.

The optical properties of $(C_6H_8N)_6InBr_9$ were investigated using UV-vis absorption and PL spectroscopy. The absorption spectrum shown in Fig. S6 (ESI†) features a broad absorption band ranging from 330 to 410 nm, which is ascribed to the electron transitions from the ground $^1S_0$ to the excited states of In^{3+} in the isolated $(InBr_6)^{3-}$ octahedron. Besides, the spectrum also contains a long tail extending up to 800 nm, which is different from those of the low-dimensional lead–halide hybrids displaying a single sharp excitonic band at absorption onset.[18,53–57] The long tail might be associated with the inter-band absorption, stemming from multiple defect states. Upon UV light excitation, $(C_6H_8N)_6InBr_9$ crystals exhibit a warm white-light emission with a color temperature of 5500 K and CIE chromaticity coordinates of (0.33, 0.37), as displayed in Fig. 2a, much closer to the standard value of (0.33, 0.33). The PL excitation (PLE) spectrum for $(C_6H_8N)_6InBr_9$ crystals shown in Fig. 2b contains two absorption peaks at ~331 and 375 nm, indicating the presence of two excited states with different energy levels. When excited at 375 nm, the PL spectrum features an ultra-broad emission band spanning from 400 to 725 nm, covering the region of warm-white light with a PLQY of ~2.72% (Fig. 2b). Note that the spectrum exhibits complex features, as it contains multiple emission peaks with the maximum one located at 544 nm, based on Gaussian fitting. This broad emission is unique and different from that of

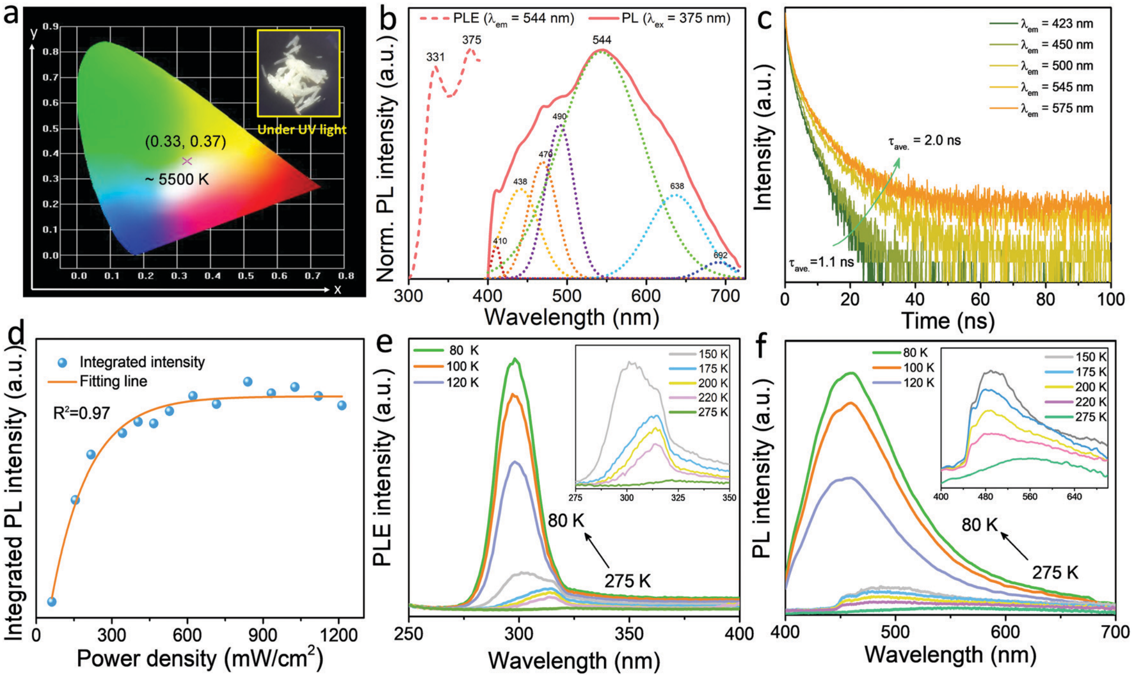

Fig. 2 (a) CIE chromaticity coordinates of the white-light emission. Inset shows the photograph of $(C_6H_8N)_6InBr_9$ crystals under 365 nm UV light. (b) PLE and PL spectra of $(C_6H_8N)_6InBr_9$. The multiple emission bands showing a dotted line are extracted by Gaussian fitting. (c) PL decay curves of $(C_6H_8N)_6InBr_9$ monitored at different emission wavelengths. (d) Integrated PL intensity *versus* excitation power for $(C_6H_8N)_6InBr_9$. Temperature-dependent PLE spectra (e) and PL spectra (f) of $(C_6H_8N)_6InBr_9$ from 80 K to 275 K.

luminescent metal-halide perovskites exhibiting single emission profiles with a Gaussian distribution stemming from the direct electron–hole, band-to-band or STE radiative recombination.[8,58–64] Considering the long absorption tail and the multiple emission peaks, the broadband white-light is tentatively attributed to emission from interband radiative recombination due to the presence of defect states. To further verify such an origin, emission-wavelength-dependent PL decay dynamics were measured; as illustrated in Fig. 2c and Table S2 (ESI†), the average lifetime monitored at different wavelengths is less than or near 2 ns and changes with increasing emission wavelength, indicating the presence of multiple emission centers with varying PL lifetimes. In addition, power-dependent PL spectra were also measured at room temperature (RT). For permanent lattice defects, the concentration of impurities is finite, meaning that the PL intensity would be saturated at high excitation power density.[55,65,66] For $(C_6H_8N)_6InBr_9$, its PL intensity saturates at high excitation power density (Fig. 2d), suggesting the origin of the white light from a defect-related excited state.

To gain more insight into the photophysical mechanism of the white light, temperature-dependent PLE/PL measurements were carried out from 275 to 80 K as shown in Fig. 2e and f. The decrease in temperature correlates with a gradual increase in the PLE intensity between 275 and 150 K and a sharp increase from 150 to 80 K. Moreover, the PLE profile narrows with temperature decreasing and the maximum PLE peak is blue-shifted to ∼300 nm at 80 K. The variation of the PLE spectrum with temperature might be on the one hand due to the reduced electron–phonon coupling that promotes excited carriers to higher energy states, and on the other hand because of the increase of the band gap. Similarly, with decreasing temperature from 275 to 80 K, the PL spectrum also exhibits an increase in intensity, narrowing of the PL profile and blue-shift of the maximum emission peak. In this case, the suppressed thermal quenching promotes radiative recombination, resulting in the increase of PL intensity; the reduced electron–phonon coupling narrows the PL profile, while the blue-shift of the PL might be due to the filling of defect states with lower energy, which has also been observed in other metal–halide perovskites.[67] For the ionic-type hybrid metal halides, shallow defects usually form in the presence of halide vacancies, which are close to the band edge, and might act as traps to localize the photogenerated carriers for radiative recombination[38,39,42,45,56,57,68] and deep-level defects within the band gap may be nonradiative recombination centers.[69–72] Previous reports indicate that intrinsic shallow defects associated with a Br vacancy (V_{Br}) can be preferentially formed in In^{3+}-based double perovskites due to their low formation energy.[73] Considering the Br-deficient nature based on energy dispersive X-ray spectroscopy characterization (Fig. S5, ESI†), the broad white-light emission of $(C_6H_8N)_6InBr_9$ can be rationally attributed to the radiative recombination from V_{Br}-related defect states.

Although white light can be achieved from defect-assisted radiative recombination in $(C_6H_8N)_6InBr_9$, the PLQY is unsatisfactory and cannot meet the application requirements. As discussed above, $(C_6H_8N)_6InBr_9$ is extremely sensitive to temperature, and its PLE/PL intensity decreases dramatically as the temperature increases, with the intensity ratio between

80 and 275 K being greater than 36 (Fig. S7, ESI†). Therefore, high room-temperature PL efficiency is expected by reducing the thermal quenching effect in $(C_6H_8N)_6InBr_9$. Generally, engineering the chemical composition or electronic structures of low-dimensional metal halides by intentionally embedding suitable extrinsic dopants is the predominant strategy for the modulation of the PL properties, both for spectral coverage and efficiency.[20,74–79] Sb^{3+} containing a stereoactive $5s^2$ lone pair not only exhibits oxidative stability and similar ionic radius (0.076 nm) to In^{3+} (0.08 nm), but also possesses efficient triplet STE states that are favorable to radiative recombination and resistant to thermal quenching. Thus in this work, Sb^{3+} was selected as the dopant to improve the PL properties of $(C_6H_8N)_6InBr_9$. As a result, Sb^{3+} has been successfully embedded into the lattice of $(C_6H_8N)_6InBr_9$ and played a significant role in manipulating the photophysical processes, enabling efficient broadband orange with a high PLQY of up to 71.84% (Fig. S8, ESI†), which greatly exceeds that of most organic–inorganic hybrid lead halides (Table S3, ESI†). The successful incorporation of Sb^{3+} in the lattice of $(C_6H_8N)_6InBr_9$ was verified by PXRD characterizations. As shown in Fig. S9 (ESI†), the PXRD pattern of $(C_6H_8N)_6InBr_9$: $3.52\%Sb^{3+}$ with the maximum Sb^{3+} content matches well with that of $(C_6H_8N)_6InBr_9$; in addition, the PXRD peaks have moved toward higher diffraction degrees due to the small radius of Sb^{3+}, confirming the successful doping of Sb^{3+}.

To shed light on the mechanism behind the enhanced PL properties, UV-vis absorption spectroscopy was carried out for Sb^{3+}-doped $(C_6H_8N)_6InBr_9$, termed as $(C_6H_8N)_6InBr_9{:}x\%Sb^{3+}$. As illustrated in Fig. S10 (ESI†), Sb^{3+}-doped $(C_6H_8N)_6InBr_9$ exhibits a similar optical absorption spectrum as compared to $(C_6H_8N)_6InBr_9$, implying that the Sb^{3+} dopant has a slight impact on the band edge, while an additional absorption peak emerges at ∼327 nm after incorporating Sb^{3+}, which is enhanced with increasing Sb^{3+} amount. Such an emerging absorption peak is attributed to the $^1S_0 \rightarrow {}^3P_1$ transition of Sb^{3+}, due to the presence of $5s^2$ electrons,[27,48,80,81] supporting the tailoring of Sb^{3+} on the material's band edge. Then, we performed density functional theory (DFT) calculations to gain more insights into the electronic properties. As presented in Fig. 3a and b, both the band structures of the undoped and Sb^{3+}-doped $(C_6H_8N)_6InBr_9$ show completely flat bands, indicating that the electronic states are highly localized. It coincides with the fact that the distance between two adjacent metal-halide octahedra are nearly 10 Å so that there is nearly no electronic coupling between them. The calculated DOSs of undoped and Sb^{3+}-doped $(C_6H_8N)_6InBr_9$ are shown in Fig. 3c and d, where the conduction band minimum (CBM) values of the undoped and Sb^{3+}-doped $(C_6H_8N)_6InBr_9$ are both contributed from In-5s and Br-4p orbitals, while the valence band maximum (VBM) of Sb^{3+}-doped $(C_6H_8N)_6InBr_9$ has a mixed Sb-5s and Br-4p character. The corresponding charge densities of the VBM and CBM for Sb^{3+}-doped $(C_6H_8N)_6InBr_9$ further confirm that charge carriers in the VBM are completely localized in the isolated $(SbBr_6)^{3-}$ octahedron, as shown in Fig. 3e, while those in the CBM are localized in the $(InBr_6)^{3-}$ octahedron (Fig. 3f). The above results verify the significant contribution of Sb^{3+} dopant to the formation of the VBM, thereby altering the photophysical processes.

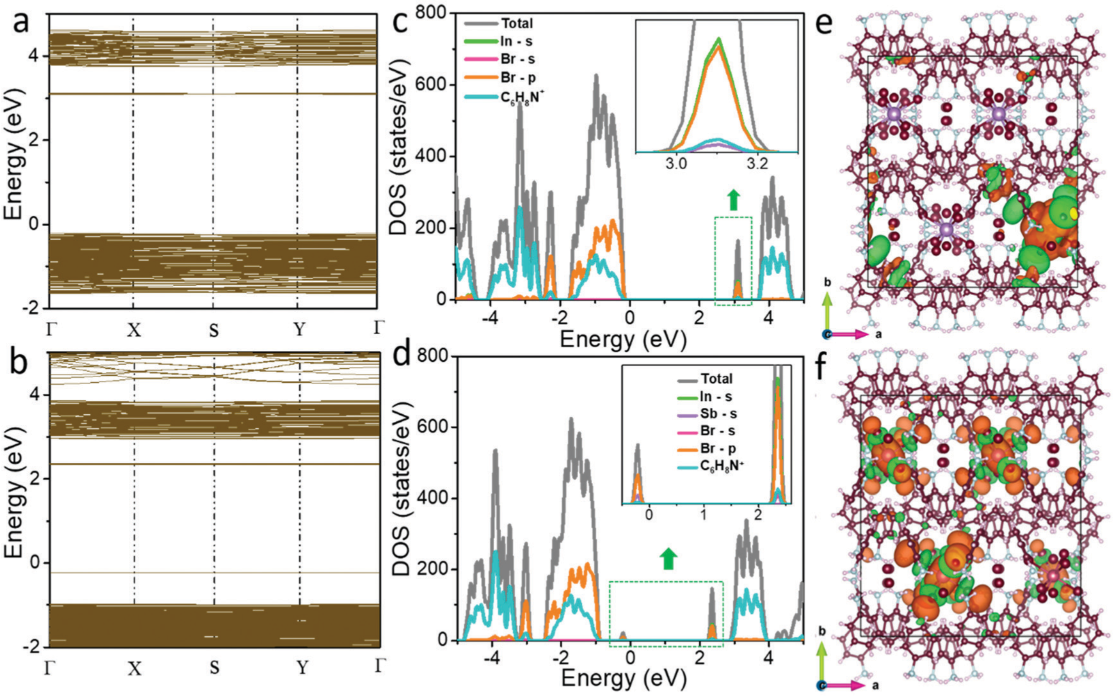

Fig. 3 Band structures of $(C_6H_8N)_6InBr_9$ (a) and Sb^{3+}-doped $(C_6H_8N)_6InBr_9$ (b), calculated by the DFT-PBE method. Total and orbital-projected DOSs for $(C_6H_8N)_6InBr_9$ (c) and Sb^{3+}-doped $(C_6H_8N)_6InBr_9$, (d) obtained with the DFT-PBE method. Charge densities of the VBM (e) and CBM (f) for Sb^{3+}-doped $(C_6H_8N)_6InBr_9$.

Experimental characterizations of Sb^{3+}-doped $(C_6H_8N)_6InBr_9$ were further carried out to elucidate the photophysical properties of the enhanced PLQY. In this study, $(C_6H_8N)_6InBr_9$:0.58%Sb with the optimal PL efficiency was selected as a prototype to reveal the mechanism behind the PL, while too much Sb^{3+} dopant will induce a concentration quenching effect (Fig. 4a and Table S4, ESI†). The actual doping amount was determined by inductively coupled plasma optical emission spectrometry (see Table S5, ESI†). As shown in Fig. 4b, two intense PLE peaks located at 322 and 365 nm have been observed for $(C_6H_8N)_6InBr_9$:0.58%Sb by monitoring at 645 nm, which are assigned to the $^1S_0 \rightarrow {}^1P_1$ and $^1S_0 \rightarrow {}^3P_1$ transitions, respectively. Upon excitation at 365 nm, a broadband PL ranging from 450 to 850 nm with a profile of near Gaussian distribution was recorded (Fig. 4b). Such a PL spectrum exhibits a large Stokes shift of 280 nm, a FWHM of up to 165 nm and a high PLQY of up to 71.84%, indicating its emission from triplet STEs of the $(SbBr_6)^{3-}$ octahedron (*i.e.*, $^3P_1 \rightarrow {}^1S_0$). The corresponding PL decay curves presented in Fig. S11 (ESI†) reveal that the average lifetime of the Sb^{3+}-doped $(C_6H_8N)_6InBr_9$ is on the microsecond scale ($\sim$1.9 μs), further supporting the emission from triplet STEs. It is a fact that the Sb^{3+}-based STE emission has a strong dependency on the crystal structure.[81] For example, in the five-coordinated antimony-halide entity, high-energy excitation succeeds in populating the high energy singlet $^1P_1$ state, leading to singlet STE emission ($^1P_1 \rightarrow {}^1S_0$) at the short wavelength region, accompanied by the thermodynamically favored triplet STE emission ($^3P_1 \rightarrow {}^1S_0$) at the long wavelength region, whereas the octahedrally coordinated antimony-halide structure will decrease the static expression of the lone pair and therefore off-centering and distortion, usually enabling high-symmetry sites and similar bond lengths, and thereby resulting in triplet STE emission from the $^3P_1$ state, with the singlet STE emission being unobserved.[82] Herein, by exciting at high energy (322 nm), no high energy singlet emission in the short wavelength region (<500 nm) is recorded (Fig. S12, ESI†), indicating the formation of a $(SbBr_6)^{3-}$ octahedron, rather than a $(SbBr_5)^{2-}$ pyramid.

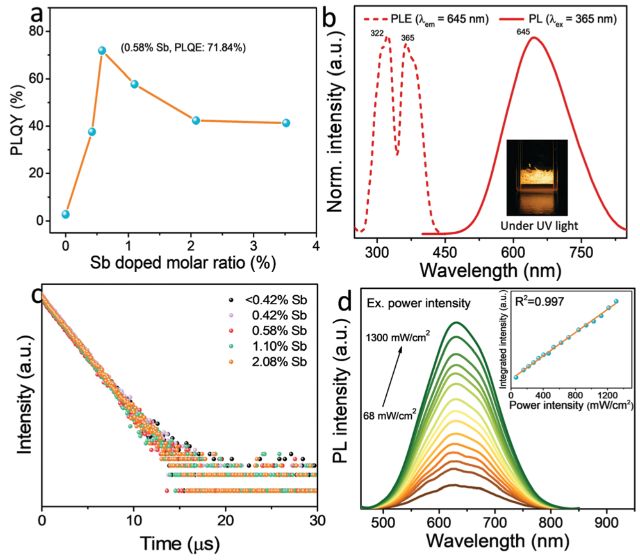

Fig. 4 (a) PLQYs of Sb^{3+}-doped $(C_6H_8N)_6InBr_9$ with different Sb^{3+} amounts. (b) PLE (λ_{em} = 645 nm) and PL (λ_{ex} = 365 nm) spectra of $(C_6H_8N)_6InBr_9$:0.58%Sb^{3+}. The inset shows the corresponding photograph of $(C_6H_8N)_6InBr_9$:0.58%Sb^{3+} crystals under 365 nm UV light. (c) PL decay curves of Sb^{3+}-doped $(C_6H_8N)_6InBr_9$ with different Sb^{3+} amounts, measured at 645 nm. (d) PL spectra of $(C_6H_8N)_6InBr_9$:0.58%Sb^{3+} recorded by varying the excitation power density. Inset shows the plots of PL intensity as a function of excitation power density.

The PL decay curves of Sb^{3+}-doped $(C_6H_8N)_6InBr_9$ with different Sb^{3+} contents exhibit identical features, indicating their similar decay dynamics induced from the Sb^{3+} dopant, as demonstrated in Fig. 4c. To eliminate the emission from lattice defects, emission/excitation-wavelength-dependent spectroscopy characterizations have been carried out; as illustrated in Fig. S13 (ESI†), both the PLE spectra monitored at various wavelengths and PL spectra excited at various wavelengths have the same features, suggesting emission from an identical emissive state. Besides, the linear dependence on excitation power density further rules out the emission from permanent lattice defects (Fig. 4d).

To better understand the mechanism of the broad emission, temperature-dependent PL measurements of $(C_6H_8N)_6InBr_9$:0.58%Sb were performed from 80 to 300 K. As shown in Fig. 5a and Fig. S14a (ESI†), the increase in temperature correlates with a slight decrease in the broadband PL intensity, with a negligible shift of the maximum PL peak. Apparently, the PL intensity of Sb^{3+}-doped $(C_6H_8N)_6InBr_9$ is insensitive to temperature, whose intensity ratio between 80 and 300 K is merely $\sim$1.68 (Fig. S14b, ESI†), much lower than that (>36) of the undoped one (Fig. S7, ESI†), verifying the negligible thermal quenching in Sb^{3+}-doped $(C_6H_8N)_6InBr_9$, thereby maintaining the high PL efficiency at RT. Furthermore, a prolonged PL lifetime (from 1.75 μs at RT to 2.11 μs at 80 K) has been witnessed for $(C_6H_8N)_6InBr_9$:0.58%Sb (Fig. S15, ESI†), implying a more efficient energy transfer of the excitons from higher to lower energy states, and eventually leading to an increase in PL intensity at low temperature. We note that the FWHM is gradually broadening, although the maximum PL peak does not shift with increasing temperature (Fig. 14a). This might be stemmed from the enhancement of thermally populated vibrational states or exciton–phonon coupling at high temperature.[35] To quantify the influence of exciton–phonon coupling on the FWHM, we have analyzed the PL line broadening with temperature using the following equation:[83]

$$\mathrm{FWHM} = 2.36\sqrt{S}\hbar\omega_{\mathrm{phonon}}\sqrt{\coth\frac{\hbar\omega_{\mathrm{phonon}}}{2k_{\mathrm{B}}T}} \tag{1}$$

the calculated Huang–Rhys factor S and $\hbar\omega_{\mathrm{phonon}}$ is about 31.16 and 26.48 meV, respectively (Fig. 5b). The resultant S outperforms most luminescent materials (Table S6, ESI†), suggesting the presence of a strong exciton–phonon coupling effect in $(C_6H_8N)_6InBr_9$:0.58%Sb, which correlates with the PL line broadening.

It is worth noting that the defect-related emission from the In–Br entity has not been detected after the incorporation of Sb^{3+} (Fig. S16, ESI†), which provides a hint of energy transfer

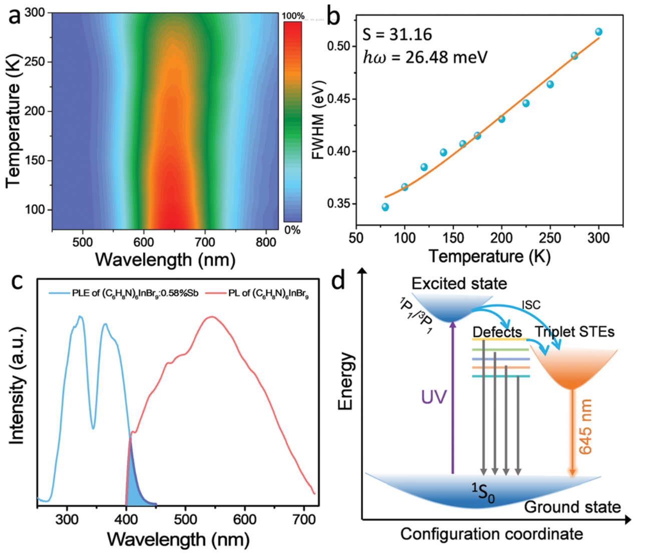

Fig. 5 (a) Temperature-dependent PL spectra measured from 80 to 300 K. (b) Experimental dependence of the FWHM broadening on temperature for $(C_6H_8N)_6InBr_9$:0.58%Sb. The FWHM values are fitted with a model, from which the Huang–Rhys factor *S* is obtained. (c) PL and PLE spectra of $(C_6H_8N)_6InBr_9$ and $(C_6H_8N)_6InBr_9$:0.58%Sb, respectively. (d) Schematic illustration of radiative channels in $(C_6H_8N)_6InBr_9$:0.58%Sb.

from the In–Br to Sb–Br entity, contributing to the enhanced triplet emission at ∼645 nm. In addition, the PLE spectrum of $(C_6H_8N)_6InBr_9$:0.58%Sb overlaps with the PL spectrum of $(C_6H_8N)_6InBr_9$, further supporting the presence of energy transfer from In–Br to the Sb–Br entity (Fig. 5c). Upon the above analysis, the possible photophysical dynamics of $(C_6H_8N)_6InBr_9$:0.58%Sb are illustrated in Fig. 5d. In brief, upon photoexcitation, electrons are promoted to the excited $^1P_1$ and $^3P_1$ states of $(SbBr_6)^{3-}$. The excited electrons in the $^1P_1$ state will experience an intersystem crossing (ISC) process to the $^3P_1$ state and then the majority of them relax to a low-energy-level triplet STE state, ultimately leading to efficient triplet STE emission with a large Stokes shift. Besides, a portion of electrons that have relaxed to the multiple defect levels of the In–Br entity will transfer to the triplet STE state due to the presence of a suitable energy difference, which contributes to the enhancement of the PL efficiency.

In addition to excellent optical properties, we have also evaluated the robustness of the materials' structural stability towards moisture and high temperature. As shown in Fig. S17a (ESI†), both the undoped and Sb^{3+}-doped $(C_6H_8N)_6InBr_9$ exhibit good humidity stability without any degradation in the PXRD patterns after storing in the air for four months. Moreover, both of them maintain structural integrity up to 170 °C (Fig. S17b, ESI†), indicating their excellent thermal stability that is important for optoelectronic applications.

Conclusions

In summary, we have successfully synthesized a novel lead-free In^{3+}-based metal halide $(C_6H_8N)_6InBr_9$ with broadband white-light emission and a PLQY of 2.72%. Such white light is attributed to the radiative recombination of excited carriers localized at shallow-defect states. Experimental results indicate that the presence of Br vacancies may serve as the radiative shallow-defect states. Interestingly, it is found that doping Sb^{3+} into $(C_6H_8N)_6InBr_9$ can effectively manipulate its electronic structure and trigger the formation of triplet excitons, resulting in a remarkable broadband emission spanning from 450 to 850 nm with a large Stokes shift of 280 nm and a FWHM of up to 165 nm. Moreover, as revealed by steady-state PL spectroscopy, energy transfer from the In–Br to Sb–Br entities may also contribute to the enhanced PL efficiency, improving the PLQY up to 71.84%. This study elucidates that radiative recombination from shallow-defect states can lead to white-light emission in metal halides in the absence of ns^2 electrons, which provide vast structural and compositional space for the design of novel materials with excellent PL performance.

Experimental section

Materials

Indium(III) bromide ($InBr_3$, Acros, 99.99%), antimony(III) bromide ($SbBr_3$, Alfa, 99.995%), and aniline (C_6H_7N, 98%) were purchased from Beijing InnoChem Science & Technology Co., Ltd (China). Hydrobromic acid (HBr, 48 wt% in water, analytical pure) was obtained from Shanghai Macklin Biochemical Co., Ltd (China). All chemicals were directly used as received.

Synthesis of $(C_6H_8N)_6InBr_9$ single crystals

$(C_6H_8N)_6InBr_9$ single crystals were prepared by a hydrothermal method. In brief, aniline and $InBr_3$ (molar ratio was 2 : 1) were dissolved in HBr solutions at room temperature (RT), respectively. Then, the above two solutions were mixed and transferred to a container and placed in a dry air oven and kept at 180 °C for 4 hours. After cooling to RT at 3 °C h^{-1}, needle like crystals were obtained. The products were filtered out, washed with fresh HBr and dried at 45 °C for 6 h. Sb^{3+}-doped samples were obtained by the same synthesis method with $SbBr_3$ and $InBr_3$ as raw materials.

Structural and spectroscopy characterizations

Single-crystal X-ray diffraction data were collected on a SuperNova E system (Agilent, America) with Cu Kα radiation (λ = 1.54184 Å) at 296 K. The material structures were solved and refined by adopting Shelxt and Olex2. Powder X-ray diffraction (PXRD) measurements were conducted by using a D2 PHASER X-ray diffractometer (Bruker, Germany). Fourier transform infrared (FTIR) spectra in the region 400–4000 cm^{-1} were recorded by using a Nicolet instrument (Thermo Fisher Scientific, Madison, WI). The steady-state photoluminescence (PL) excitation, PL emission spectra, time-resolved PL and power density-dependent PL spectra were obtained on a Florolog-3 fluorescence spectrometer (Horiba, America). Temperature-dependent PL was measured using an FLS1000 fluorescence spectrophotometer (Edinburgh Instruments Ltd, UK). UV-vis absorption spectroscopy of the samples was carried out on a Cary5000 instrument (Agilent, Malaysia). The morphology and energy dispersive X-ray spectroscopy (EDX) were examined on a Quattro S instrument (Thermo Science). Thermogravimetric analysis was conducted at a heating rate of 10 °C min^{-1} to 600 °C by using a TGA550 instrument (TA, America) under a N_2 atmosphere.

Computational methods

Density functional theory calculations of $(C_6H_8N)_6InBr_9$ and Sb^{3+}-doped $(C_6H_8N)_6InBr_9$ are carried out using the Vienna *ab initio* simulation package (VASP)[84,85] by considering projected augmented wave (PAW)[86] and generalized gradient approximation (GGA).[87] The electronic exchange function is described by the Perdew–Burke–Emzerhof (PBE) exchange–correlation functional. In order to get a more accurate electronic structure, the total energy SCF convergence value was set to 1×10^{-6} eV per atom, using a basis set of the force convergence less than 0.02 eV Å^{-1}, and the plane wave cutoff energy was 400 eV for calculations. The Monkhorst–Pack *k*-point mesh of the Brillouin zone was selected as $1 \times 1 \times 1$ to calculate the supercells of $2 \times 1 \times 1$ $(C_6H_8N)_6InBr_9$ and Sb^{3+}-doped $(C_6H_8N)_6InBr_9$, where Sb^{3+} just replaces an In^{3+} in the supercell.

Conflicts of interest

There are no conflicts to declare.

Acknowledgements

We acknowledge the financial support from the National Natural Science Foundation of China (52172154, 22109130), the Fundamental Research Funds for the Central Universities (SWU 119067), the Natural Science Foundation of Chongqing (cstc2020jcyj-msxmX0332, cstc2021jcyj-msxm2853), and Program for Innovation Team Building at Institutions of Higher Education in Chongqing (CXTDX201601011).

Notes and references

1 J. J. Yoo, G. Seo, M. R. Chua, T. G. Park, Y. Lu, F. Rotermund, Y.-K. Kim, C. S. Moon, N. J. Jeon, J.-P. Correa-Baena, V. Bulović, S. S. Shin, M. G. Bawendi and J. Seo, *Nature*, 2021, **590**, 587–593.

2 X. Jiang, F. Wang, Q. Wei, H. Li, Y. Shang, W. Zhou, C. Wang, P. Cheng, Q. Chen, L. Chen and Z. Ning, *Nat. Commun.*, 2020, **11**, 1245.

3 B. Liu, H. Bi, D. He, L. Bai, W. Wang, H. Yuan, Q. Song, P. Su, Z. Zang, T. Zhou and J. Chen, *ACS Energy Lett.*, 2021, **6**, 2526–2538.

4 W. Xu, Q. Hu, S. Bai, C. Bao, Y. Miao, Z. Yuan, T. Borzda, A. J. Barker, E. Tyukalova, Z. Hu, M. Kawecki, H. Wang, Z. Yan, X. Liu, X. Shi, K. Uvdal, M. Fahlman, W. Zhang, M. Duchamp, J.-M. Liu, A. Petrozza, J. Wang, L.-M. Liu, W. Huang and F. Gao, *Nat. Photonics*, 2019, **13**, 418–424.

5 S. Yakunin, M. Sytnyk, D. Kriegner, S. Shrestha, M. Richter, G. J. Matt, H. Azimi, C. J. Brabec, J. Stangl, M. V. Kovalenko and W. Heiss, *Nat. Photonics*, 2015, **9**, 444–449.

6 Y. Zhang, R. Sun, X. Ou, K. Fu, Q. Chen, Y. Ding, L.-J. Xu, L. Liu, Y. Han, A. V. Malko, X. Liu, H. Yang, O. M. Bakr, H. Liu and O. F. Mohammed, *ACS Nano*, 2019, **13**, 2520–2525.

7 J. Luo, L. Yang, Z. Tan, W. Xie, Q. Sun, J. Li, P. Du, Q. Xiao, L. Wang, X. Zhao, G. Niu, L. Gao, S. Jin and J. Tang, *Adv. Mater.*, 2021, **33**, 2101903.

8 Z. Ma, Z. Shi, D. Yang, Y. Li, F. Zhang, L. Wang, X. Chen, D. Wu, Y. Tian, Y. Zhang, L. Zhang, X. Li and C. Shan, *Adv. Mater.*, 2021, **33**, 2001367.

9 L. Zhou, J. F. Liao, Z. G. Huang, J. H. Wei, X. D. Wang, H. Y. Chen and D. B. Kuang, *Angew. Chem., Int. Ed.*, 2019, **58**, 15435.

10 R. Zhang, X. Mao, Y. Yang, S. Yang, W. Zhao, T. Wumaier, D. Wei, W. Deng and K. Han, *Angew. Chem., Int. Ed.*, 2019, **58**, 2725–2729.

11 B. M. Benin, D. N. Dirin, V. Morad, M. Worle, S. Yakunin, G. Raino, O. Nazarenko, M. Fischer, I. Infante and M. V. Kovalenko, *Angew. Chem., Int. Ed.*, 2018, **57**, 11329–11333.

12 M. D. Smith, B. A. Connor and H. I. Karunadasa, *Chem. Rev.*, 2019, **119**, 3104–3139.

13 C. Peng, Z. Zhuang, H. Yang, G. Zhang and H. Fei, *Chem. Sci.*, 2018, **9**, 1627–1633.

14 C. Zhou, H. Lin, H. Shi, Y. Tian, C. Pak, M. Shatruk, Y. Zhou, P. Djurovich, M. H. Du and B. Ma, *Angew. Chem., Int. Ed.*, 2018, **57**, 1021–1024.

15 J. Li, T. Inoshita, T. Ying, A. Ooishi, J. Kim and H. Hosono, *Adv. Mater.*, 2020, e2002945, DOI: 10.1002/adma.202002945.

16 R. Gautier, F. Massuyeau, G. Galnon and M. Paris, *Adv. Mater.*, 2019, **31**, e1807383.

17 Z. Zhang, R. Zhao, S. Teng, K. Huang, L. Zhang, D. Wang, W. Yang, R. Xie and N. Pradhan, *Small*, 2020, **16**, 2004272.

18 H. Yuan, F. Massuyeau, N. Gautier, A. B. Kama, E. Faulques, F. Chen, Q. Shen, L. Zhang, M. Paris and R. Gautier, *Angew. Chem., Int. Ed.*, 2020, **59**, 2802–2807.

19 S. Yakunin, B. M. Benin, Y. Shynkarenko, O. Nazarenko, M. I. Bodnarchuk, D. N. Dirin, C. Hofer, S. Cattaneo and M. V. Kovalenko, *Nat. Mater.*, 2019, **18**, 846–852.

20 J. Luo, X. Wang, S. Li, J. Liu, Y. Guo, G. Niu, L. Yao, Y. Fu, L. Gao, Q. Dong, C. Zhao, M. Leng, F. Ma, W. Liang, L. Wang, S. Jin, J. Han, L. Zhang, J. Etheridge, J. Wang, Y. Yan, E. H. Sargent and J. Tang, *Nature*, 2018, **563**, 541–545.

21 V. Morad, Y. Shynkarenko, S. Yakunin, A. Brumberg, R. D. Schaller and M. V. Kovalenko, *J. Am. Chem. Soc.*, 2019, **141**, 9764–9768.

22 J.-H. Wei, J.-F. Liao, X.-D. Wang, L. Zhou, Y. Jiang and D.-B. Kuang, *Matter*, 2020, **3**, 892–903.

23 Z. Wang, Z. Zhang, L. Tao, N. Shen, B. Hu, L. Gong, J. Li, X. Chen and X. Huang, *Angew. Chem., Int. Ed.*, 2019, **58**, 9974–9978.

24 Z. Wang, D. Xie, F. Zhang, J. Yu, X. Chen and C. P. Wong, *Sci. Adv.*, 2020, **6**, eabc2181.

25 Q. He, C. Zhou, L. Xu, S. Lee, X. Lin, J. Neu, M. Worku, M. Chaaban and B. Ma, *ACS Mater. Lett.*, 2020, **2**, 633–638.

26 M. D. Smith and H. I. Karunadasa, *Acc. Chem. Res.*, 2018, **51**, 619–627.

27 H. Arfin, A. S. Kshirsagar, J. Kaur, B. Mondal, Z. Xia, S. Chakraborty and A. Nag, *Chem. Mater.*, 2020, **32**, 10255–10267.

28 H. Lin, C. Zhou, Y. Tian, T. Siegrist and B. Ma, *ACS Energy Lett.*, 2017, **3**, 54–62.

29 M. I. Saidaminov, O. F. Mohammed and O. M. Bakr, *ACS Energy Lett.*, 2017, **2**, 889–896.

30 L. Zhou, J.-F. Liao and D.-B. Kuang, *Adv. Opt. Mater.*, 2021, **9**, 2100544.

31 M. Li and Z. Xia, *Chem. Soc. Rev.*, 2021, **50**, 2626–2662.

32 J. S. Manser, J. A. Christians and P. V. Kamat, *Chem. Rev.*, 2016, **116**, 12956–13008.

33 Z. Li, C. Zhang, B. Li, C. Lin, Y. Li, L. Wang and R.-J. Xie, *Chem. Eng. J.*, 2021, **420**, 129740.

34 C. Zhou, H. Lin, M. Worku, J. Neu, Y. Zhou, Y. Tian, S. Lee, P. Djurovich, T. Siegrist and B. Ma, *J. Am. Chem. Soc.*, 2018, **140**, 13181–13184.

35 C. Zhou, H. Lin, Y. Tian, Z. Yuan, R. Clark, B. Chen, L. J. van de Burgt, J. C. Wang, Y. Zhou, K. Hanson, Q. J. Meisner, J. Neu, T. Besara, T. Siegrist, E. Lambers, P. Djurovich and B. Ma, *Chem. Sci.*, 2018, **9**, 586–593.

36 S. Seth, T. Ahmed, A. De and A. Samanta, *ACS Energy Lett.*, 2019, **4**, 1610–1618.

37 F. Ambrosio, E. Mosconi, A. A. Alasmari, F. A. S. Alasmary, D. Meggiolaro and F. De Angelis, *Chem. Mater.*, 2020, **32**, 6916–6924.

38 X. Wu, M. T. Trinh, D. Niesner, H. Zhu, Z. Norman, J. S. Owen, O. Yaffe, B. J. Kudisch and X. Y. Zhu, *J. Am. Chem. Soc.*, 2015, **137**, 2089–2096.

39 I. Spanopoulos, I. Hadar, W. Ke, P. Guo, E. M. Mozur, E. Morgan, S. Wang, D. Zheng, S. Padgaonkar, G. N. Manjunatha Reddy, E. A. Weiss, M. C. Hersam, R. Seshadri, R. D. Schaller and M. G. Kanatzidis, *J. Am. Chem. Soc.*, 2021, **143**, 7069–7080.

40 D. Cortecchia, S. Neutzner, A. R. Srimath Kandada, E. Mosconi, D. Meggiolaro, F. De Angelis, C. Soci and A. Petrozza, *J. Am. Chem. Soc.*, 2017, **139**, 39–42.

41 G. Wu, C. Zhou, W. Ming, D. Han, S. Chen, D. Yang, T. Besara, J. Neu, T. Siegrist, M.-H. Du, B. Ma and A. Dong, *ACS Energy Lett.*, 2018, **3**, 1443–1449.

42 G. M. Paternò, N. Mishra, A. J. Barker, Z. Dang, G. Lanzani, L. Manna and A. Petrozza, *Adv. Funct. Mater.*, 2019, **29**, 1805299.

43 X. Li, X. Lian, J. Pang, B. Luo, Y. Xiao, M.-D. Li, X.-C. Huang and J. Z. Zhang, *J. Phys. Chem. Lett.*, 2020, **11**, 8157–8163.

44 J. Zhou, M. Li, L. Ning, R. Zhang, M. S. Molokeev, J. Zhao, S. Yang, K. Han and Z. Xia, *J. Phys. Chem. Lett.*, 2019, **10**, 1337–1341.

45 Z. Tan, J. Li, C. Zhang, Z. Li, Q. Hu, Z. Xiao, T. Kamiya, H. Hosono, G. Niu, E. Lifshitz, Y. Cheng and J. Tang, *Adv. Funct. Mater.*, 2018, **28**, 1801131.

46 G. Volonakis, A. A. Haghighirad, R. L. Milot, W. H. Sio, M. R. Filip, B. Wenger, M. B. Johnston, L. M. Herz, H. J. Snaith and F. Giustino, *J. Phys. Chem. Lett.*, 2017, **8**, 772–778.

47 P. Han, C. Luo, S. Yang, Y. Yang, W. Deng and K. Han, *Angew. Chem., Int. Ed.*, 2020, **59**, 12709–12713.

48 Y. Jing, Y. Liu, X. Jiang, M. S. Molokeev, Z. Lin and Z. Xia, *Chem. Mater.*, 2020, **32**, 5327–5334.

49 L. Zhou, J.-F. Liao, Z.-G. Huang, J.-H. Wei, X.-D. Wang, W.-G. Li, H.-Y. Chen, D.-B. Kuang and C.-Y. Su, *Angew. Chem., Int. Ed.*, 2019, **58**, 5277–5281.

50 Z. Li, G. Song, Y. Li, L. Wang, T. Zhou, Z. Lin and R.-J. Xie, *J. Phys. Chem. Lett.*, 2020, **11**, 10164–10172.

51 J.-H. Wei, J.-F. Liao, L. Zhou, J.-B. Luo, X.-D. Wang and D.-B. Kuang, *Sci. Adv.*, 2021, **7**, eabg3989.

52 D. Chen, S. Hao, G. Zhou, C. Deng, Q. Liu, S. Ma, C. Wolverton, J. Zhao and Z. Xia, *Inorg. Chem.*, 2019, **58**, 15602–15609.

53 J. Yin, R. Naphade, L. Gutiérrez Arzaluz, J.-L. Brédas, O. M. Bakr and O. F. Mohammed, *ACS Energy Lett.*, 2020, **5**, 2149–2155.

54 A. Biswas, R. Bakthavatsalam, S. R. Shaikh, A. Shinde, A. Lohar, S. Jena, R. G. Gonnade and J. Kundu, *Chem. Mater.*, 2019, **31**, 2253–2257.

55 E. R. Dohner, A. Jaffe, L. R. Bradshaw and H. I. Karunadasa, *J. Am. Chem. Soc.*, 2014, **136**, 13154–13157.

56 D. Cortecchia, S. Neutzner, A. R. Srimath Kandada, E. Mosconi, D. Meggiolaro, F. De Angelis, C. Soci and A. Petrozza, *J. Am. Chem. Soc.*, 2017, **139**, 39–42.

57 X. Li, X. Lian, J. Pang, B. Luo, Y. Xiao, M. D. Li, X. C. Huang and J. Z. Zhang, *J. Phys. Chem. Lett.*, 2020, **11**, 8157–8163.

58 L. Protesescu, S. Yakunin, M. I. Bodnarchuk, F. Krieg, R. Caputo, C. H. Hendon, R. X. Yang, A. Walsh and M. V. Kovalenko, *Nano Lett.*, 2015, **15**, 3692–3696.

59 X. Li, Y. Wang, H. Sun and H. Zeng, *Adv. Mater.*, 2017, **29**, 1701185.

60 A. D. Wright, C. Verdi, R. L. Milot, G. E. Eperon, M. A. Perez-Osorio, H. J. Snaith, F. Giustino, M. B. Johnston and L. M. Herz, *Nat. Commun.*, 2016, **7**, 11755.

61 S. Yuan, Z.-K. Wang, L.-X. Xiao, C.-F. Zhang, S.-Y. Yang, B.-B. Chen, H.-T. Ge, Q.-S. Tian, Y. Jin and L.-S. Liao, *Adv. Mater.*, 2019, **31**, 1904319.

62 X. Zhang, C. Wang, Y. Zhang, X. Zhang, S. Wang, M. Lu, H. Cui, S. V. Kershaw, W. W. Yu and A. L. Rogach, *ACS Energy Lett.*, 2018, **4**, 242–248.

63 C. Ji, S. Wang, L. Li, Z. Sun, M. Hong and J. Luo, *Adv. Funct. Mater.*, 2019, **29**, 1805038.

64 T. Jun, K. Sim, S. Iimura, M. Sasase, H. Kamioka, J. Kim and H. Hosono, *Adv. Mater.*, 2018, **30**, e1804547.

65 S. Tongay, J. Suh, C. Ataca, W. Fan, A. Luce, J. S. Kang, J. Liu, C. Ko, R. Raghunathanan, J. Zhou, F. Ogletree, J. Li, J. C. Grossman and J. Wu, *Sci. Rep.*, 2013, **3**, 2657.

66 T. Schmidt, K. Lischka and W. Zulehner, *Phys. Rev. B: Condens. Matter Mater. Phys.*, 1992, **45**, 8989–8994.

67 H.-H. Fang, R. Raissa, M. Abdu-Aguye, S. Adjokatse, G. R. Blake, J. Even and M. A. Loi, *Adv. Funct. Mater.*, 2015, **25**, 2378–2385.

68 J. Yin, H. Yang, K. Song, A. M. El-Zohry, Y. Han, O. M. Bakr, J.-L. Brédas and O. F. Mohammed, *J. Phys. Chem. Lett.*, 2018, **9**, 5490–5495.

69 X.-K. Liu, W. Xu, S. Bai, Y. Jin, J. Wang, R. H. Friend and F. Gao, *Nat. Mater.*, 2021, **20**, 10–21.

70 J. Yin, G. H. Ahmed, O. M. Bakr, J.-L. Brédas and O. F. Mohammed, *ACS Energy Lett.*, 2019, **4**, 789–795.

71 A. B. Wong, Y. Bekenstein, J. Kang, C. S. Kley, D. Kim, N. A. Gibson, D. Zhang, Y. Yu, S. R. Leone, L.-W. Wang, A. P. Alivisatos and P. Yang, *Nano Lett.*, 2018, **18**, 2060–2066.

72 T. Xuan and R.-J. Xie, *Chem. Eng. J.*, 2020, **393**, 124757.

73 J. Xu, J. B. Liu, B. X. Liu and B. Huang, *J. Phys. Chem. Lett.*, 2017, **8**, 4391–4396.

74 J. Yu, J. Kong, W. Hao, X. Guo, H. He, W. R. Leow, Z. Liu, P. Cai, G. Qian, S. Li, X. Chen and X. Chen, *Adv. Mater.*, 2019, **31**, e1806385.

75 B. M. Benin, K. M. McCall, M. Wörle, V. Morad, M. Aebli, S. Yakunin, Y. Shynkarenko and M. V. Kovalenko, *Angew. Chem., Int. Ed.*, 2020, **59**, 14490–14497.

76 K. M. McCall, C. C. Stoumpos, O. Y. Kontsevoi, G. C. B. Alexander, B. W. Wessels and M. G. Kanatzidis, *Chem. Mater.*, 2019, **31**, 2644–2650.

77 Y. Zhou, J. Chen, O. M. Bakr and H.-T. Sun, *Chem. Mater.*, 2018, **30**, 6589–6613.

78 Y. Liu, X. Rong, M. Li, M. S. Molokeev, J. Zhao and Z. Xia, *Angew. Chem., Int. Ed.*, 2020, **59**, 11634–11640.

79 C. Wang, Y. Liu, Y. Guo, L. Ma, Y. Liu, C. Zhou, X. Yu and G. Zhao, *Chem. Eng. J.*, 2020, **397**, 125367.

80 Z. Li, Y. Li, P. Liang, T. Zhou, L. Wang and R.-J. Xie, *Chem. Mater.*, 2019, **31**, 9363–9371.

81 K. M. McCall, V. Morad, B. M. Benin and M. V. Kovalenko, *ACS Mate. Lett.*, 2020, **2**, 1218–1232.

82 A. Vogler and H. Nikol, *Comments Inorg. Chem.*, 1993, **14**, 245–261.

83 W. Stadler, D. M. Hofmann, H. C. Alt, T. Muschik, B. K. Meyer, E. Weigel, G. Müller-Vogt, M. Salk, E. Rupp and K. W. Benz, *Phys. Rev. B: Condens. Matter Mater. Phys.*, 1995, **51**, 10619–10630.

84 G. Kresse and J. Furthmüller, *Comput. Mater. Sci.*, 1996, **6**, 15–50.

85 G. Kresse and J. Furthmüller, *Phys. Rev. B: Condens. Matter Mater. Phys.*, 1996, **54**, 11169–11186.

86 G. Kresse and D. Joubert, *Phys. Rev. B: Condens. Matter Mater. Phys.*, 1999, **59**, 1758–1775.

87 J. P. Perdew, K. Burke and M. Ernzerhof, *Phys. Rev. Lett.*, 1996, **77**, 3865–3868.